Preprints of the 22nd IFAC World Congress
Yokohama, Japan, July 9-14, 2023

Modeling-free Learning Control of Cross-coupled Fast Steering Mirror for 2-D Trajectory

Shingo Ito* ** Ernst Csencsics Georg Schitter****

* *Department of Mechanical Engineering, University of Fukui, 3-9-1 Bunkyo, Fukui, 910-8507, Japan (e-mail: ito@u-fukui.ac.jp).*
** *Automation and Control Institute (ACIN), TU Wien, Vienna A-1040, Austria.*

Abstract: This paper proposes modeling-free inversion-based iterative control (MF-IIC) for a fast steering mirror, which is a dual-input dual-output system to generate 2-D optical scanning trajectories. To explicitly compensate for the cross-coupling motions, the MF-IIC iteratively updates the control inputs by learning from the previous trials based on a 2×2 Jacobian matrix. To operate the MF-IIC without system identification in advance, it estimates the Jacobian matrix including the non-diagonal elements for the cross-coupling dynamics simultaneously during learning. For experiments, 19 Hz and 20 Hz sine waves with an amplitude of 0.65° are used for a Lissajous pattern as a reference trajectory. Experimental results show that a tracking error of 320×10^{-3} degrees when feedback control is used for stability. By additionally combing the proposed MF-IIC, the error is decreased by a factor of 68 to 4.64×10^{-3} degrees. It is smaller than MF-IIC without considering the cross coupling explicitly, which achieves a tracking error of 12.1×10^{-3} deg. These two MF-IIC algorithms are also compared by the resulting sampled trajectories in the spatial domain. For that purpose, maximum dead zone diameter is defined as a diameter of the largest circle without sampled points in a scanning area in this paper. While the MF-IIC without considering the cross coupling explicitly for comparison creates a Lissajous pattern with a maximum dead zone diameter of 74.8×10^{-3} degrees, the proposed MF-IIC achieves a Lissajous pattern with a smaller maximum dead zone diameter of 72.9×10^{-3} degrees, demonstrating its effectiveness for high-quality scanning trajectories.

Keywords: Mechatronic systems, Motion control systems, Scanners, Learning algorithms.

1. INTRODUCTION

Two dimensional (2-D) scanning of an optical or laser spot is utilized for instrumentation (e.g. confocal microscopy [Pawley (2006)]) and manufacturing such as laser cutting and 3D printing [Stampfl et al. (2016)]. To increase the throughput of these applications, 2-D scanners with a higher scanning speed are desired without impairing the precision and accuracy of optical trajectories.

A typical scanner configuration is shown in Fig. 1(left), where a pair of galvanometer scanners are used to scan an optical spot over a target surface along the x and y axes. Galvanometer scanners consist of a shaft with a mirror that reflects a beam for scanning. The shaft is typically supported by bearings and rotated by electromagnetic actuators [Matsuka et al. (2016)]. Due to the structure of such galvanometer scanners, their control challenges typically include the bearing friction and mechanical resonances of the shaft and the mirror. To compensate them for high-speed, high-precision scanning trajectories, control algorithms such as repetitive control (RC) [Shih and Chen (2022)], iterative learning control (ILC) [Yoo et al. (2016)], and inversion-based iterative control (IIC) [Ito et al. (2020a)] have been applied.

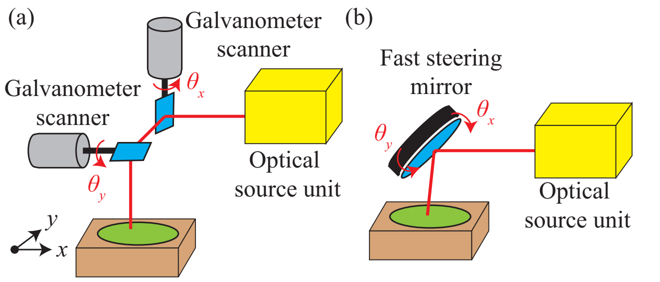

Fig. 1. 2-D laser scanning system with (a) galvanometer scanners and (b) a fast steering mirror.

An advantage of galvanometer scanners is their large rotation angle, which is typically more than ±10° in the case of off-the-shelf scanners. It is another advantage that the x- and y-axis rotations are physically decoupled. However, when two galvanometer scanners are configured for 2-D scanning, they are relatively bulky. This is problematic when a compact 2-D scanner is required, for example for robot-based inline metrology, where a 3-D imaging system with a 2-D scanner is mounted onto an industrial robot to optimize production settings in a line [Wertjanz et al. (2022)].

As shown in Fig. 1(right), 2-D scanners can be compact by using a fast steering mirror (FSM), or tip-tilt mirror. Although its rotational angle is typically a few degrees or less, its size is advantageous especially when a relatively large mirror is desired, for example for a high numerical aperture or a small optical spot. A FSM uses a mirror that is typically suspended by flexures and tilted around two orthogonal axes by actuators for 2-D optical trajectories. Dependent on requirements on the bandwidth and the rotation angle, piezoelectric actuators [Zhong et al. (2022)], Lorentz actuators [Xiao et al. (2019)], or hybrid reluctance actuators (HRA) [Csencsics et al. (2019)] can be selected. Especially by using hybrid reluctance actuators (HRAs), a relatively large rotation angle and high bandwidth can be simultaneously realized [Csencsics and Schitter (2021)]. However, HRAs have control challenges such as a nonlinearity due to position-dependent forces [Ito et al. (2019)] and a phase lag due to eddy currents. Furthermore, cross coupling of the x-axis and y-axis angles occurs as an additional challenge. To overcome these challenges, motion control is indispensable.

Control algorithms such as RC [Tang et al. (2019a)], disturbance observer [Tang et al. (2019b)], and ILC [Dong et al. (2018)] are applied to FSMs. Some of them are targeted for disturbance rejection, and they are usually designed based on a plant model. For 2-D scanning by a FSM with HRAs, however, control algorithms that require no plant model are desired because of the complexity to accurately model the plant with the HRA's nonlinearities and the cross-coupling dynamics.

To realize fast and precise scanning trajectories, this paper proposes modeling-free inversion-based iterative control (MF-IIC) for a FSM, which is a dual-input dual-output (DIDO) system. Similar to ILC, IIC iteratively updates control inputs by learning from the data in the previous trials. However, IIC learns in the frequency domain. MF-IIC utilizes the characteristics and simultaneously carries out system identification with the collected data in the frequency domain. Consequently, no plant model is required in design. The proposed MF-IIC explicitly takes the cross coupling of the DIDO system into account. To validate its effectiveness, scanning trajectories are evaluated not only in the time domain, but also in the spatial domain by the size of dead zones without data points on a image.

2. SYSTEM DESCRIPTION

Fig. 2 shows a FSM used in this paper, and a similar FSM is presented in detail in [Csencsics et al. (2019)]. The mirror is supported by flexures and bearing balls. Tip-tilt motions of the mirror are created by a 2-D HRA, which consists of coils, a permanent magnet, and ferromagnetic materials for reluctance forces. The HRA is driven by current amplifiers for coil currents, and their reference currents are denoted by v_x and v_y in Fig. 3. The mirror angles θ_x and θ_y are measured by using multiple eddy-current displacement sensors in the FSM.

Fig. 4 shows measured frequency response functions (FRFs) from v_x and v_y to θ_x and θ_y in open loop. The FRFs from v_x to θ_x and from v_y to θ_y exhibit typical dynamics of a damped mass-spring system, due to the mirror suspended by the flexures and the bearing balls for the x- and y-axis

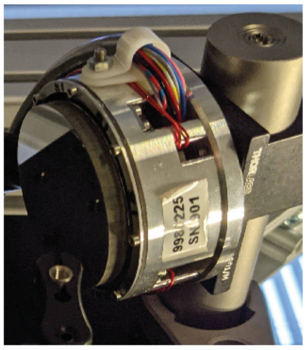

Fig. 2. Photograph of a FSM for experiments.

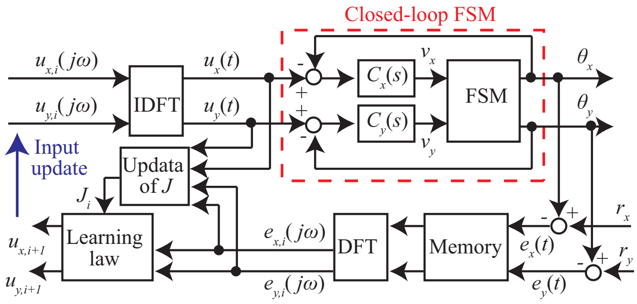

Fig. 3. Block diagram of the FSM controlled by feedback controllers and MF-IIC.

rotations. The other FRFs from v_x to θ_y and from v_y to θ_x show the cross-coupling dynamics of the two axis rotations. The cross-coupling motions are relatively small by design. It is less than 40 dB, or 1 % (Fig. 4), at low frequencies below 80 Hz. However, the cross-coupling motions increase around the mechanical resonant frequency (app. 100 Hz).

To compensate for the cross coupling around the resonant frequency and also for position-dependent forces of the HRA, feedback control is utilized. Due the relatively small cross coupling, two SISO controllers $C_x(s)$ and $C_y(s)$ are used, as shown in Fig. 3. They are designed such that the achievable open-loop crossover frequency is 250 Hz with a sufficient phase margin of more than 40°. The feedback controllers are implemented by a rapid prototyping control system (DS1005, dSpace GmbH, Paderborn, Germany) at a sampling frequency of 20 kHz.

For MF-IIC design in the next section, FRFs of the resulting closed-loop system are described by

$$\begin{bmatrix} \theta_x(j\omega) \\ \theta_y(j\omega) \end{bmatrix} = \begin{bmatrix} P_{xx}(j\omega) & P_{xy}(j\omega) \\ P_{yx}(j\omega) & P_{yy}(j\omega) \end{bmatrix} \begin{bmatrix} u_x(j\omega) \\ u_y(j\omega) \end{bmatrix}, \quad (1)$$

where $u_x(j\omega)$ and $u_y(j\omega)$ are regarded as the control inputs to the closed-loop system (Fig. 3), and $P_{n,m}(s)$ is a corresponding SISO FRF. For validation of the feedback control design, FRFs of the closed-loop FSM are measured in Fig. 5, where the mechanical resonance near 100 Hz results in deep magnitude notches for good decoupling rotations of the mirror.

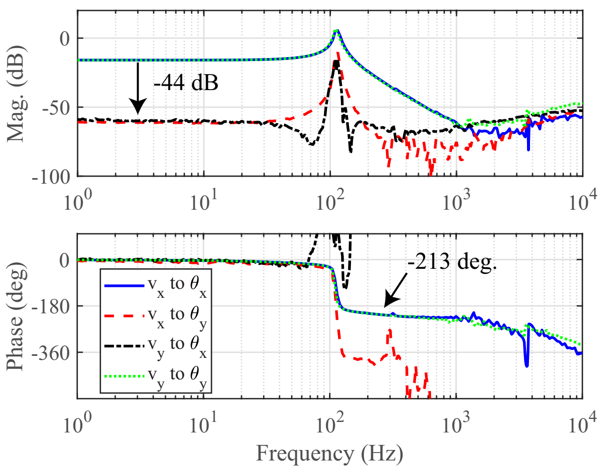

Fig. 4. Measured frequency response of the FSM in open loop, where the cross-coupling motions are less than -40 dB (1 %).

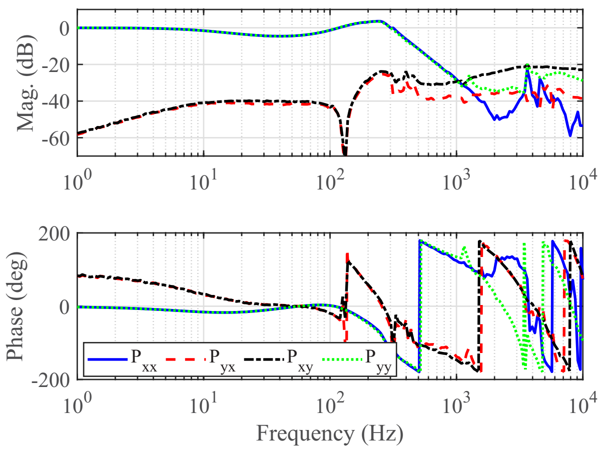

Fig. 5. Measured frequency response of the closed-loop system from u_x and u_y to θ_x and θ_y.

3. DESIGN OF MODELING-FREE IIC

As a 2-D scanning trajectory of an optical spot, a Lissajous scan is selected for an advantage that a preview of a sample is available for imaging applications [Tuma et al. (2013)]. For the trajectory, the reference signal r_x of the x-axis rotation is a sine wave with an amplitude of 0.65° and a frequency of 19 Hz. Similarly, a 20 Hz sine wave with the same amplitude is used as the reference signal r_y of the y-axis rotation (see Fig. 7(a)). With these settings, a Lissajous scan is completed in a second to distribute its sampled data points in an area of 1.3°×1.3° (see Fig. 9).

To track the reference trajectory, Fig. 3 also shows a block diagram of MF-IIC. To learn in the frequency domain, the measured mirror angles $\theta_x(t)$ and $\theta_y(t)$ for a second are stored in a memory for discrete Fourier transform. The transformed signals $\theta_{x,i}(j\omega)$ and $\theta_{y,i}(j\omega)$, where the subscript i denotes the number of iteration, are fed to learning algorithms that update the control inputs to $u_{x,i+1}(j\omega)$ and $u_{y,i+1}(j\omega)$. They are transformed to time-domain signals by inverse DFT (IDFT) for the next learning iteration.

A learning law of MF-IIC [Kim and Zou (2013); Zhang and Zou (2022)] for SISO systems is extended for a DIDO system. For that purpose, $\theta_{x,i}(j\omega)$ and $\theta_{y,i}(j\omega)$ are differentiated with respect to i

$$\frac{\mathrm{d}}{\mathrm{d}i}\begin{bmatrix}\theta_{x,i}\\ \theta_{y,i}\end{bmatrix} = J_i \begin{bmatrix}\dfrac{\mathrm{d}u_{x,i}}{\mathrm{d}i}\\ \dfrac{\mathrm{d}u_{y,i}}{\mathrm{d}i}\end{bmatrix}, \tag{2}$$

where J_i is a Jacobian matrix. Eq. (2) is rewritten in a discrete form

$$\begin{bmatrix}\theta_{x,i+1}\\ \theta_{y,i+1}\end{bmatrix} - \begin{bmatrix}\theta_{x,i}\\ \theta_{y,i}\end{bmatrix} = J_i\left(\begin{bmatrix}u_{x,i+1}\\ u_{y,i+1}\end{bmatrix} - \begin{bmatrix}u_{x,i}\\ u_{y,i}\end{bmatrix}\right). \tag{3}$$

To enable precise tracking motions at the $i+1$-th iteration, the first term of the left-hand side is replaced by the reference trajectory in (3), and the following learning law is obtained:

$$\begin{bmatrix}u_{x,i+1}\\ u_{y,i+1}\end{bmatrix} = \begin{bmatrix}u_{x,i}\\ u_{y,i}\end{bmatrix} + J_i^{-1}\begin{bmatrix}e_{x,i}\\ e_{y,i}\end{bmatrix}, \tag{4}$$

where $e_{x,i} = r_x - \theta_{x,i}$ and $e_{y,i} = r_y - \theta_{y,i}$ are tracking errors. Note that the learning law has a form of the Newton-Raphson method [Verbeke and Cools (1995)].

The Jacobian matrix is given by

$$J_i = \begin{bmatrix} j_{xx,i} & j_{xy,i}\\ j_{yx,i} & j_{yy,i}\end{bmatrix} = \begin{bmatrix}\dfrac{\partial\theta_{x,i}}{\partial u_{x,i}} & \dfrac{\partial\theta_{x,i}}{\partial u_{y,i}}\\ \dfrac{\partial\theta_{y,i}}{\partial u_{x,i}} & \dfrac{\partial\theta_{y,i}}{\partial u_{y,i}}\end{bmatrix}. \tag{5}$$

In the case of linear systems, J_i corresponds to the FRF matrix in (1). For model-based IIC, it is obtained by system identification in advance and utilized in (4) for learning. In this paper, J_i is iteratively estimated during learning for modeling-free or data-driven IIC, and the Secant method is selected, for its excellent performances at least in the case of a SISO system [Ito et al. (2017)]. To extend it for the DIDO system, the following two methods are compared:

3.1 SISO MF-IIC

Due to the well-decoupled design of the FSM in Sec. 2, the cross coupling of the mirror rotations can be neglected in IIC design [Yan et al. (2012)]. To take advantage of the characteristics for simplicity, the following law is used to update J_i:

$$j_{xx,i} = \begin{cases}\dfrac{\theta_{x,i}-\theta_{x,i-1}}{u_{x,i}-u_{x,i-1}} & \text{for } |u_{x,i}-u_{x,i-1}| \geq \epsilon,\\ j_{xx,i-1} & \text{otherwise,}\end{cases}$$

$$j_{yy,i} = \begin{cases}\dfrac{\theta_{y,i}-\theta_{y,i-1}}{u_{y,i}-u_{y,i-1}} & \text{for } |u_{y,i}-u_{y,i-1}| \geq \epsilon,\\ j_{yy,i-1} & \text{otherwise,}\end{cases}$$

$$j_{xy,i} = j_{yx,i} = 0, \tag{6}$$

where ϵ is a threshold for stable learning and tuned a small value at the implementation.

As the diagonal element of the Jacobian matrix is always zero, the resulting MF-IIC does not explicitly take account of the cross-coupling motions. Furthermore, the learning law (4) and the update law (6) are activated only at the fundamental frequencies of the sine waves (19 Hz and 20 Hz) and their harmonic frequencies. This enables to filter the measurement noise in-between for high-precision scanning motions in the case of SISO systems such as a galvanometer scanner [Ito et al. (2020b)]. Because two MF-IIC for SISO systems are running for the x- and y-axis rotations independently, this method is referred to as SISO MF-IIC hereafter.

3.2 DIDO MF-IIC

As the second method, the paper proposes a sub step i_s to update the control inputs u_x and u_y not simultaneously, but individually. In the transition from the $i-1$-th step to the sub step i_s, only the control input u_x is updated in Fig. 3, and the mirror angles are measured at the sub step as θ_{x,i_s} and θ_{y,i_s}. They are used to update two Jacobian elements as follows

$$j_{xx,i} = \begin{cases} \dfrac{\theta_{x,i_s} - \theta_{x,i-1}}{u_{x,i} - u_{x,i-1}} & \text{for } |u_{x,i} - u_{x,i-1}| \geq \epsilon, \\ j_{xx,i-1} & \text{otherwise,} \end{cases}$$

$$j_{yx,i} = \begin{cases} \dfrac{\theta_{y,i_s} - \theta_{y,i-1}}{u_{x,i} - u_{x,i-1}} & \text{for } |u_{x,i} - u_{x,i-1}| \geq \epsilon, \\ j_{xy,i-1} & \text{otherwise.} \end{cases}$$

Similarly, only the control input u_y is updated in the transition from the sub step i_s to the i-th step. The mirror angles measured at the i-th step are used to update the other elements of J_i as follows

$$j_{xy,i} = \begin{cases} \dfrac{\theta_{x,i} - \theta_{x,i_s}}{u_{y,i} - u_{y,i-1}} & \text{for } |u_{y,i} - u_{y,i-1}| \geq \epsilon, \\ j_{yy,i-1} & \text{otherwise,} \end{cases}$$

$$j_{yy,i} = \begin{cases} \dfrac{\theta_{y,i} - \theta_{y,i_s}}{u_{y,i} - u_{y,i-1}} & \text{for } |u_{y,i} - u_{y,i-1}| \geq \epsilon, \\ j_{yy,i-1} & \text{otherwise.} \end{cases}$$

The above method needs more time and memory for the measurements and their DFT at the sub step. However, the cross coupling of the mirror rotations is explicitly compensated by the estimated non-diagonal elements $j_{xy,i}$ and $j_{yx,i}$. For convenience, the method is referred to as DIDO MF-IIC hereafter. Because the 2-D trajectory has a period of 1 s, DIDO MF-IIC is activated at the fundamental frequency (1 Hz) and its harmonic frequencies. The matrix J_i is an internal non-parametric model, and it corresponds to the FRF matrix of the plant in the case of a linear system. Thus, the above Jacobian matrix estimation is regarded as an internal system identification based on the data corrected for learning.

4. EXPERIMENTS IN THE TIME DOMAIN

For experiments of SISO MF-IIC and DIDO MF-IIC, a 2×2 identity matrix is used as the initial condition of J_i. Similarly, r_x and r_y are used as the initial condition of $u_{x,i}$ and $u_{y,i}$, respectively. With these settings, the mirror rotations at $i=0$ are regulated by the feedback controllers only. To evaluate tracking errors of the 2-axis rotations by a single value, a total RMS error

$$e_t = \sqrt{e_{x,rms}^2 + e_{y,rms}^2} \tag{7}$$

is used, where $e_{x,rms}$ and $e_{y,rms}$ are the tracking errors of the x and y axes in RMS, respectively.

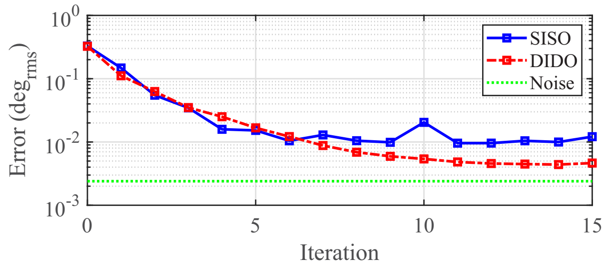

Fig. 6. Comparison of learning transient, where the green line indicates the level of noise included in the measured angles. The vertical axis shows the total RMS error e_t in (7).

Fig. 6 compares resulting learning transient, successfully demonstrating stable learning of both SISO and DIDO MF-IIC. The total RMS error is 0.32° at $i=0$, where the FSM is controlled by feedback control only. SISO MF-IIC significantly decreases the relatively large error by a factor of 26 to 12.1×10^{-3} deg. However, the residual error is larger than noise included in θ_x and θ_y that is 2.40 $\times10^{-3}$ deg. This implies possibility to further decrease the tracking error. In fact, Fig. 7(b) shows that the residual error e_x of SISO MF-IIC is periodic at $i=15$.

In Fig. 6, DIDO MF-IIC shows a better tracking performance by decreasing the tracking error by a factor of 68 to 4.64×10^{-3} deg. at $i=15$, which is close to the noise of 2.40 $\times10^{-3}$ deg. The superior performance is also clearly visible in the time domain. The tracking error e_x of DIDO MF-IIC in Fig. 7(c) is almost half of SISO MF-IIC in Fig. 7(b). Overall, the experimental comparison reveals that the proposed sub step approach to explicitly compensate for the cross-coupling motions are effective for a high-precision scanning trajectory.

5. EVALUATION IN THE SPACIAL DOMAIN

5.1 Maximum dead zone diameter

The achieved trajectories are evaluated in the time domain in the previous section. However, evaluation of trajectories in the spacial domain is also desired, for example to determine for imaging resolution in the case of microscope applications. To evaluate sampled scanning trajectories, this paper defines "maximum dead zone diameter" as the maximum diameter of circles that contain no sampled points in a scanning area. Maximum dead zone diameters can be used for opto-mechatronic system design. For example, to detect all the features in an area by confocal microscopy, the maximum dead zone diameter should be less than or equal to the laser diameter. Otherwise, there exist regions that are not scanned by the laser, where features are overlooked. To calculate maximum dead zone diameters, this paper proposes to use a voronoi diagram for given sampled points of a trajectory.

In a voronoi diagram, a cell is assigned to each sampled point such that any location on a cell is closer to the corresponding point than to the others [Cheng et al. (2010)]. In Fig. 8(left), the sampled points of a trajectory are indicated by blue squares, and black lines are borders of polygon cells as an example. Due to the cell assignment,

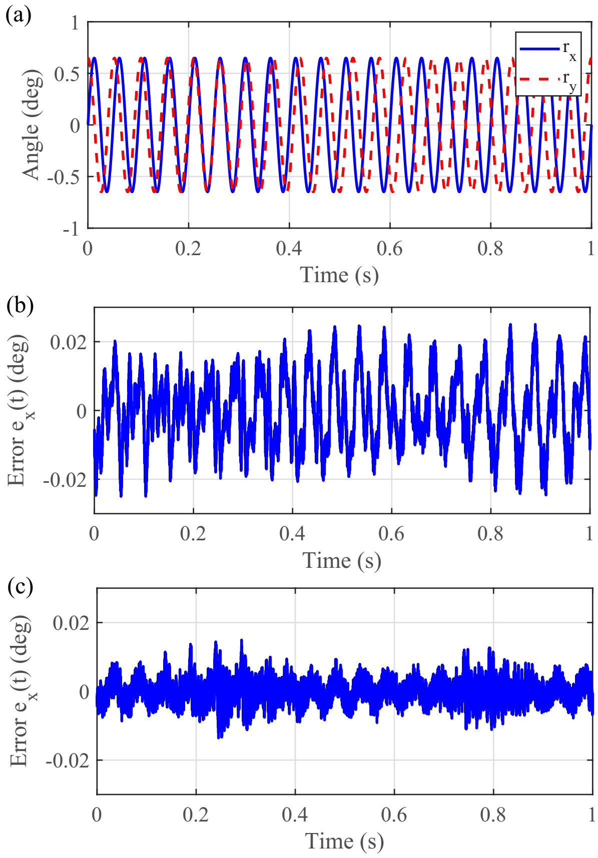

Fig. 7. Trajectories in the time domain at $i = 15$: (a) reference trajectories r_x and r_y, (b) Tracking error e_x of SISO MF-IIC, and (c) e_x of DIDO MF-IIC. For similarity, e_y is omitted in this paper.

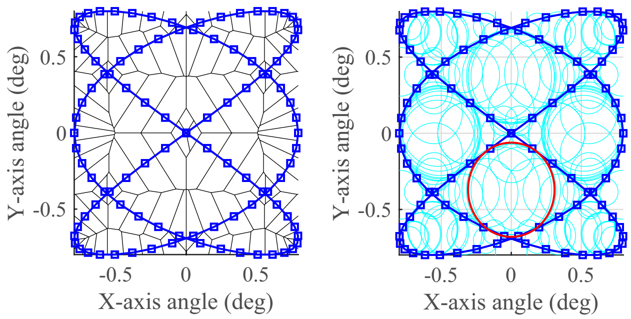

Fig. 8. (Left) Voronoi cells calculated for a sampled Lissajous trajectory, and (Right) circular dead zones that contain no sampled points, where the red circle indicates the largest one.

distances from a point on a cell border to two adjacent sampled points are equal. Similarly, distances from a vertex of a cell are equal to three adjacent sampled points at least. Thus, these distances are a radius of a circular dead zone without sampled points. Fig. 8(right) shows circular dead zones found from the cells' vertices. For the maximum dead zone diameter, the largest dead zone is identified by the red circle in Fig. 8(right).

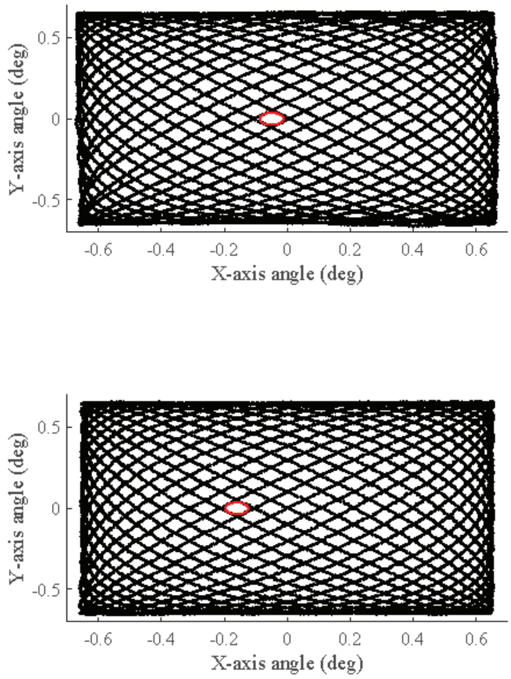

Fig. 9. Measured mirror angles θ_x and θ_y, where red circles indicate the largest circular dead zone. (Top) SISO MF-IIC and (Bottom) DIDO MF-IIC.

5.2 *Trajectory evaluation*

For evaluation in the spacial domain, the trajectories achieved by SISO and DIDO MF-IIC at $i = 15$ in Sec. 4 are shown in Fig. 9. In the case of SISO MF-IIC in Fig. 9(top), the Lissajous trajectory is deformed by the tracking errors, particularly around the corners. This might be because the rotational speed becomes zero at the corners, where stiction of the bearing balls occurs as a nonlinear disturbance. The red circle indicates the largest circular dead zone, and its diameter (i.e. maximum dead zone diameter) is 74.8×10^{-3} deg. The deformation is compensated by DIDO MF-IIC in Fig. 9(bottom), where the maximum dead zone diameter is successfully decreased to 72.9×10^{-3} deg.

In summary, the influence of the cross coupling of the mirror rotations are clearly visible in both the time domain and the spatial domain although the FSM is well-designed even with feedback control and SISO MF-IIC. The proposed DIDO MF-IIC successfully decreases the remaining tracking errors without a plant model, which is realized by the internal system identification algorithms to estimate the system dynamics including the cross coupling.

6. CONCLUSION

To enable high-quality 2-D scanning trajectories, this paper proposes MF-IIC for a FSM, which is a DIDO system. To compensate for the problematic cross coupling of the mirror rotations, the proposed MF-IIC estimates a 2×2 Jacobian matrix and updates the control inputs iteratively. For the estimation of the non-diagonal elements of the matrix, which explicitly capture the cross-coupling dynamics, the control inputs for the x- and y-axis rotations are individually updated, and the resulting trajectories are measured. For demonstration, the FSM tracks a Lissajous trajectory that consists of 19 Hz and 20 Hz sine waves with an amplitude of 0.65°. The experimental results in the time domain reveal that the proposed MF-IIC decreases the tracking errors of the FSM with feedback control by a factor of 68. Furthermore, the residual errors are less than half of MF-IIC designed without considering the cross coupling for comparison, demonstrating the effectiveness of the proposed MF-IIC.

To evaluate scanning trajectories in the spatial domain, the paper additionally proposes maximum dead zone diameter, which is the maximum diameter of circular dead zones in a scanning area. The MF-IIC designed without considering the cross coupling creates a Lissajous pattern with a maximum dead zone diameter of 74.8×10^{-3} deg. The proposed MF-IIC successfully decreases it to 72.9×10^{-3} deg. Overall, the experimental results in the time domain and the spatial domain demonstrate the importance and effectiveness of the explicit cross-coupling compensation by estimating the non-diagonal elements of the Jacobian matrix for high-quality scanning trajectories. Future work includes analysis on convergence properties.

REFERENCES

Cheng, R., Xie, X., Yiu, M.L., Chen, J., and Sun, L. (2010). Uv-diagram: A voronoi diagram for uncertain data. In *2010 IEEE 26th International Conference on Data Engineering (ICDE 2010)*, 796–807. doi: 10.1109/ICDE.2010.5447917.

Csencsics, E., Schlarp, J., Schopf, T., and Schitter, G. (2019). Compact high performance hybrid reluctance actuated fast steering mirror system. *Mechatronics*, 62, 102251.

Csencsics, E. and Schitter, G. (2021). Exploring the pareto fronts of actuation technologies for high performance mechatronic systems. *IEEE/ASME Transactions on Mechatronics*, 26(2), 1053–1063.

Dong, Q., Liu, Y., Zhang, Y., Gao, S., and Chen, T. (2018). Improved adrc with ilc control of a ccd-based tracking loop for fast steering mirror system. *IEEE Photonics Journal*, 10(4), 1–14. doi: 10.1109/JPHOT.2018.2846287.

Ito, S., Poik, M., Csencsics, E., Schlarp, J., and Schitter, G. (2020a). High-speed scanning chromatic confocal sensor for 3-D imaging with modeling-free learning control. *Appl. Opt.*, 59(29), 9234–9242.

Ito, S., Troppmair, S., Lindner, B., Cigarini, F., and Schitter, G. (2019). Long-range fast nanopositioner using nonlinearities of hybrid reluctance actuator for energy efficiency. *IEEE Transactions on Industrial Electronics*, 66(4), 3051–3059.

Ito, S., Woong Yoo, H., and Schitter, G. (2020b). Noise reduction of learning control for periodic motion of galvanometer scanner. *IFAC-PapersOnLine*, 53(2), 8401–8406. 21st IFAC World Congress.

Ito, S., Yoo, H.W., and Schitter, G. (2017). Comparison of modeling-free learning control algorithms for galvanometer scanner's periodic motion. In *IEEE International Conference on Advanced Intelligent Mechatronics*, 1357–1362.

Kim, K.S. and Zou, Q. (2013). A modeling-free inversion-based iterative feedforward control for precision output tracking of linear time-invariant systems. *IEEE/ASME Transactions on Mechatronics*, 18(6), 1767–1777.

Matsuka, D., Tanaka, T., and Iwasaki, M. (2016). Thermal demagnetization compensation for fast and precise positioning in galvanometer scanners. *IEEE Transactions on Industrial Electronics*, 63(9), 5514–5522.

Pawley, J. (2006). *Handbook of Biological Confocal Microscopy*. Springer US, 3 edition. doi:10.1007/978-0-387-45524-2.

Shih, L.W. and Chen, C.W. (2022). Model-free repetitive control design and implementation for dynamical galvanometer-based raster scanning. *Control Engineering Practice*, 122, 105124.

Stampfl, J., Liska, R., and Ovsianikov, A. (2016). *Multiphoton Lithography: Techniques, Materials and Applications*. Wiley-VCH.

Tang, T., Xu Niu, S., Yang, T., Qi, B., and Liang Bao, Q. (2019a). Vibration rejection of tip-tilt mirror using improved repetitive control. *Mechanical Systems and Signal Processing*, 116, 432–442.

Tang, T., Niu, S., Chen, X., and Qi, B. (2019b). Disturbance observer-based control of tip-tilt mirror for mitigating telescope vibrations. *IEEE Transactions on Instrumentation and Measurement*, 68(8), 2785–2791.

Tuma, T., Sebastian, A., Lygeros, J., and Pantazi, A. (2013). The four pillars of nanopositioning for scanning probe microscopy: The position sensor, the scanning device, the feedback controller, and the reference trajectory. *IEEE Control Systems Magazine*, 33(6), 68–85.

Verbeke, J. and Cools, R. (1995). The newton-raphson method. *International Journal of Mathematical Education in Science and Technology*, 26(2), 177–193.

Wertjanz, D., Kern, T., Pechhacker, A., Csencsics, E., and Schitter, G. (2022). Robotic precision 3D measurements in vibration-prone environments enabled by active six dof sample-tracking. In *IEEE/ASME International Conference on Advanced Intelligent Mechatronics*, 1441–1446.

Xiao, R., Xu, M., Shao, S., and Tian, Z. (2019). Design and wide-bandwidth control of large aperture fast steering mirror with integrated-sensing unit. *Mechanical Systems and Signal Processing*, 126, 211–226.

Yan, Y., Wang, H., and Zou, Q. (2012). A decoupled inversion-based iterative control approach to multi-axis precision positioning: 3d nanopositioning example. *Automatica*, 48(1), 167–176.

Yoo, H.W., Ito, S., and Schitter, G. (2016). High speed laser scanning microscopy by iterative learning control of a galvanometer scanner. *Control Engineering Practice*, 50, 12–21.

Zhang, Z. and Zou, Q. (2022). Optimal data-driven difference-inversion-based iterative control: High-speed nanopositioning tracking example. *IEEE Transactions on Control Systems Technology*, 1–11.

Zhong, J., Nishida, R., and Shinshi, T. (2022). Design and precision tracking control of a high-bandwidth fast steering mirror for laser beam machining. *Precision Engineering*, 73, 128–139.